JGR Atmospheres

RESEARCH ARTICLE
10.1029/2024JD041502

A Statistical Study of Polar Mesospheric Cloud Fronts in the Northern Hemisphere

Brentha Thurairajah[1], Chihoko Y. Cullens[2], V. Lynn Harvey[2,3], and Cora E. Randall[2,3]

[1]Bradley Department of Electrical and Computer Engineering, Center for Space Science and Engineering Research, Blacksburg, VA, USA, [2]Laboratory for Atmospheric and Space Physics, University of Colorado Boulder, Boulder, CO, USA, [3]Department of Atmospheric and Oceanic Sciences, University of Colorado, Boulder, CO, USA

Key Points:

- Polar mesospheric cloud (PMC) images from satellite data are used to identify fronts that separate cloud from mostly clear regions
- Near-coincident temperature profiles indicate the presence of inversion layers at PMC altitudes
- Ducted gravity waves in some of the temperature inversions may have supported the formation of PMC fronts

Correspondence to:

B. Thurairajah,
brenthat@vt.edu

Citation:

Thurairajah, B., Cullens, C. Y., Harvey, V. L., & Randall, C. E. (2024). A Statistical study of polar mesospheric cloud fronts in the northern hemisphere. *Journal of Geophysical Research: Atmospheres*, *129*, e2024JD041502. https://doi.org/10.1029/2024JD041502

Received 1 MAY 2024
Accepted 23 SEP 2024

Abstract Complex spatial structures in polar mesospheric cloud (PMC) images provide visual clues to the dynamics that occur in the summer mesosphere. In this study, we document one such structure, a PMC front, by analyzing PMC images in the northern hemisphere from the Cloud Imaging and Particle Size (CIPS) instrument onboard the aeronomy of ice in the mesosphere (AIM) satellite. A PMC front is defined as a sharp boundary that separates cloudy and mostly clear regions, and where the clouds at the front boundary are brighter than the clouds in the cloudy region. We explore the environment that supports the formation of PMC fronts using near-coincident temperature and water vapor observations from the Sounding of the Atmosphere using Broadband Emission Radiometry (SABER) satellite instrument. A comparison of PMC front locations to near-coincident temperature profiles reveals the presence of inversion layers at PMC altitudes. The adiabatic and superadiabatic topside lapse rates of these temperature inversions indicate that some of the identified inversion layers may have been formed by gravity wave (GW) dissipation. The structure of the squared buoyancy frequency profiles indicates a stable layer or thermal duct that can be associated with large-amplitude mesospheric inversion layers (MILs) that extend large distances. These inversion layers may be conducive to horizontal wave propagation. We hypothesize that ducted GWs may be a formation mechanism of PMC fronts.

Plain Language Summary Polar mesospheric clouds (PMCs) are high-altitude (~80–90 km) clouds that form at high latitudes in the summer, when water vapor freezes to ice. The CIPS instrument on the AIM satellite provides images of these clouds that reveal complex structures. We characterize one of these structures as PMC fronts. In the troposphere, a front separates air masses with different temperatures. Similarly, a PMC front separates cloudy regions and mostly clear regions that have large temperature differences. Using near-coincident data from the SABER instrument, the fronts are identified to be located in the presence of temperature inversion layers. In the mesosphere, the temperature generally decreases with altitude. An inversion layer occurs when the temperature increases with increasing altitude due to factors such as wave breaking. Based on the inversion layer characteristics, we theorize that some of these temperature inversions may have created an environment that supports the formation of PMC fronts.

1. Introduction

The mesosphere is an important region of the atmosphere where intricate wave processes couple the dynamic upper atmosphere with wave sources near the Earth's surface. Some of the inner workings of the mesosphere can be studied via visual clues provided by polar mesospheric clouds (PMCs). PMCs (also referred to as Noctilucent Clouds (NLCs), when viewed from the ground) are high-altitude clouds (~80–90 km) (Hervig et al., 2013; Karlsson et al., 2009) that occur in the high-latitude summer mesosphere but have also been observed at mid-latitudes (e.g., Russell et al., 2014). PMC images have revealed both complex spatial structures and unique morphological forms including veils, bands, billows, whirls (Gadsden & Parviainen, 1996) and other structures such as ice voids, fronts, and vortex like structures (e.g., Dalin et al., 2013; Fritts et al., 2020; Thurairajah, Bailey, Nielsen, et al., 2013). These structures, which are usually signatures of atmospheric gravity waves (GWs), turbulence, or Kelvin Helmholtz instability provide important clues to the dynamics of the mesosphere and associated vertical coupling processes that control the summer mesosphere.

Previous studies of mesospheric cloud images have mostly focused on the ubiquitous band structures associated with GWs (e.g., Chandran et al., 2009; Dalin et al., 2004; Zhao et al., 2015). In this paper, we focus on the 'front'-like structure in PMCs, defined as a solitary wave or a sharp step-like boundary that separates cloudy and mostly clear regions in the mesosphere. Previous case studies on mesospheric fronts (Dalin et al., 2013; Dubietis

et al., 2011; Thurairajah et al., 2021) have reported a significant temperature difference ($\Delta T \approx 20$ K) across the cloud and clear regions. This structure is referred to as a 'front' because in the troposphere, a front separates air masses with different density or temperature. A modeling study by Dong et al. (2021) suggest a relation between PMC fronts and ice voids (Megner et al., 2018; Rusch et al., 2009; Thurairajah, Bailey, Siskind, et al., 2013). Dong et al. (2021) noted that "localized GW packets can yield a range of influences on PMCs at spatial scales", including the formation of ice voids from GW packets exhibiting strong self-acceleration dynamics and instability dynamics and the formation of 'fronts' from the leading edge of a GW packet.

Dalin et al. (2013) used NLC photographs and Thurairajah et al. (2021) used PMC images from the Cloud Imaging and Particle Size (CIPS) instrument on the Aeronomy of Ice in the Mesosphere (AIM; Russell et al., 2009) satellite to report case studies of a PMC front structure. Using coincident satellite temperature observations, both studies reported that the temperature difference across cloudy and clear regions was due to the presence of a mesospheric inversion layer (MIL). A MIL is a layer between the stratopause and mesopause in which the temperature is warmer than the surrounding air. That is, contrary to standard behavior in the mesosphere, on the bottom layer of an MIL, the temperature increases with altitude. MILs have been observed at all latitudes (e.g., Gan et al., 2012; Irving et al., 2014; Merriwether & Gerrard, 2004). Proposed mechanisms for increasing the temperature to form an MIL include GW breaking (e.g., Liu et al., 2000), planetary wave breaking and dissipation (e.g., France et al., 2015; Irving et al., 2014; Oberheide et al., 2006; Salby et al., 2002), GW-tide interaction (States & Gardner, 2000), and chemical heating (Meriwether & Mlynczak, 1995; Ramesh et al., 2014). Dalin et al. (2013) and Thurairajah et al. (2021) suggested that given the visual similarity between PMC fronts and mesospheric bores observed in airglow images in the upper mesosphere (~90–100 km), an MIL that forms a duct for bore propagation may also be responsible for the solitary wave and sharp boundary along a PMC front.

A mesospheric bore is a propagating front that is usually followed by a wave train or turbulence (e.g., Dewan & Picard, 1998; Pautet et al., 2018; Ramachandran et al., 2023; Yue et al., 2010). A bore requires a ducting region to propagate in it. This ducting region can be produced by wind shear that forms a Doppler duct, a temperature inversion layer that forms a thermal duct, or a combination of both wind shear and temperature inversion layer that forms a thermal-Doppler duct (Dewan & Picard, 2001; Hozumi et al., 2019; Simkhada et al., 2009; Smith et al., 2005). Thermal ducts occur when the squared buoyancy frequency varies with altitude in such a way that a stable layer is surrounded by unstable layers, thus preventing vertical wave propagation. Ducted waves tend to be quasi-monochromatic but also exhibit trailing wave crests as they propagate inside the duct and dissipate.

Thurairajah et al. (2021) presented a case study of the PMC front observed by CIPS on 2 July 2007 over Greenland. This front structure had the appearance of a solitary wave with no trailing waves. The front and the weakening of the sharp boundary was identified in three successive orbits, with the front structure diminishing in the third orbit. Given the 90 min cadence between the CIPS orbits in the northern hemisphere 2007 PMC season, this structure was estimated to be propagating at a speed of 60 m/s and to have a lifetime of at least 90 min. Thurairajah et al. (2021) identified coincident observations of temperature and water vapor over the cloudy and clear regions separated by the front from the Sounding of the Atmosphere using Broadband Emission Radiometry (SABER) measurements (Russell et al., 1999). At 84 km altitude, the temperature in the cloudy region was 136 K. In the clear region, where a MIL was present, the temperature was 156 K. The authors concluded that the higher temperatures in the MIL destroyed clouds, resulting in the clear region. Thurairajah et al. (2021) speculated that a thermal duct created by a temperature enhancement that was still small enough for the region to support cloud formation may have enabled the formation of a solitary ducted wave, resulting in the formation of the observed PMC front. Moreover, large amplitude GWs with tropospheric sources were identified to have contributed to the formation of the MIL.

In this paper, we extend the study by Thurairajah et al. (2021) to identify several PMC front structures and coincident temperature and water vapor observations from 15 years CF of satellite data. We focus on observations in the northern hemisphere (NH). Section 2 describes the data and methodology. Section 3 describes general characteristics of PMC fronts, presents a case study of a PMC front, and characteristics of coincident temperature inversion layers. Section 4 includes a summary and conclusion.

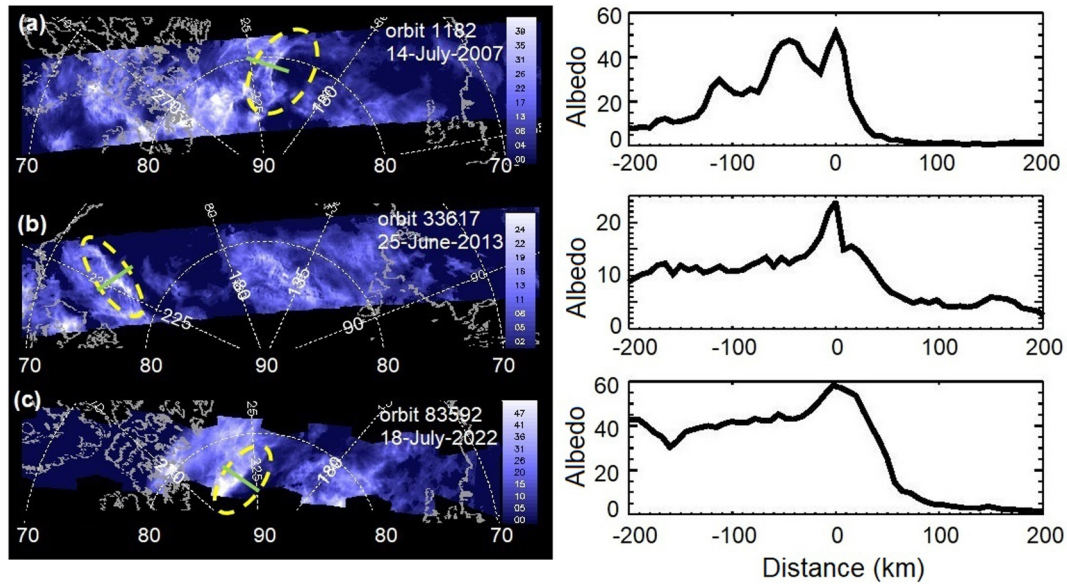

Figure 1. (left) Example of PMC front structures as observed by CIPS (highlighted in yellow) on (a) 14 July 2007, (b) 25 June 2013, and (c) 18 July 2022. (right) Albedo in units of 1×10^{-6} sr^{-1} as a function of distance along the transect (green line in PMC images) across the front. The distance from the peak albedo at zero km is positive in the mostly clear region and negative in the cloudy region.

2. Data and Methodology

2.1. PMC Fronts From AIM/CIPS Images

CIPS is a 4-camera panoramic imager (McClintock et al., 2009) that measured scattered UV atmospheric radiance throughout sunlit latitudes on a daily basis from May 2007 to March 2023. Signatures of mesospheric clouds at polar and mid-latitudes are inferred from CIPS images in the NH from approximately mid-May to late August and in the southern hemisphere (SH) from approximately mid-November to mid-February (e.g., Benze et al., 2009, 2011; Rusch et al., 2009; Thurairajah, Bailey, Nielsen, et al., 2013). With a 4-camera field of view of about 1,000 km × 2,000 km (across-track x along-track typically), image acquisition approximately every 2 to 3 min, and 15 orbits per day, CIPS mapped nearly the entire summer polar cap each day during PMC seasons with a horizontal resolution of 56 km^2. Poleward of about 70° latitude the orbits overlapped, leading to multiple observations of a single location that was separated in time by about 90 min. For the results presented here, it is important to note that no PMC data are available for the NH 2017 PMC season because of a lack of calibration data. More details of the CIPS instrument as well as the CIPS PMC retrieval algorithm and error analysis are described in Bailey et al. (2009), Carstens et al. (2013), and Lumpe et al. (2013).

In this study, we identify front structures using CIPS Level 2, version 5.20 rev 05 PMC data from the NH 2007–2022 PMC seasons. Each level 2 data file pertains to a single orbit for which all CIPS images acquired during that orbit have been combined into a single orbit "strip", examples of which are shown in Figure 1. Thus, where PMCs are present on the sunlit portion of each orbit, the CIPS level 2 data display a continuous measure of the PMC albedo, which is defined as the measured radiance divided by the input solar irradiance. Note that the continuous display was disrupted from early 2016 to 2018, when the CIPS image orientation rotated by ~90° due to rapid changes in satellite beta angle, resulting in less overlap between successive images in a single orbit.

Structures that are characterized as potential PMC fronts are first identified visually from albedo orbit strips as features that appear to have a sharp, bright cloud boundary separating cloudy and mostly clear regions. Then, a scan across the center of, and nearly perpendicular to, the sharp cloud boundary is drawn manually for each potential front. A potential front is then identified as an actual front only if the scan exhibits a sharp boundary between the cloudy and mostly clear regions, and if the cloud albedo along the boundary is significantly higher than the albedo within the adjacent cloudy region (see below for quantitative details). Figures 1a–1c show examples of PMC fronts in CIPS images from AIM orbits 1182 (14 July 2007), 33617 (25 June 2013), and 83592 (18

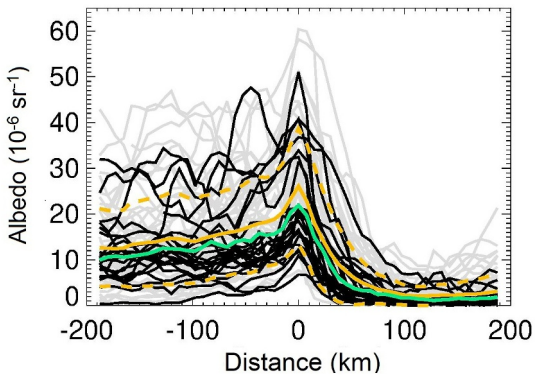

Figure 2. Transects of cloud albedo across 73 front structures. (black) CIPS cloud albedo along the transects across the 24 front structures in the vicinity of the SABER near-coincident temperature measurements. (gray) CIPS cloud albedo along the transects across the 49 transects that were not coincident with SABER data. The distance from the peak albedo at zero km is positive in the mostly clear region and negative in the cloudy region. The mean (solid orange), one standard deviation (dashed orange) and the median (green) of the 73 transects are also shown.

July 2022). The albedo variation across the front structures, shown in the right panels of Figure 1 as plots of albedo along the transects (green lines, left panel) versus distance from the fronts, illustrates the morphology of the fronts. This morphology includes the sharp drop in the albedo value from the cloudy to mostly clear regions and the decrease in albedo from the bright cloud edge to relatively dim clouds in the cloudy region.

From the transects of visually recognized front structures, 73 PMC fronts were identified from the NH 2007–2022 PMC seasons in independent, non-overlapping, non-consecutive, orbit strips. We acknowledge that since front identification required visual analysis of thousands of orbit strips, there is a subjective component to the results reported here. However, given the challenges in identifying potential fronts and appropriate transects electronically, no automated front identification algorithm exists yet. The 73 identified fronts are likely only a small subset of the actual number of fronts present, but we believe that we have captured the most robust fronts that are representative of the larger population. Figure 2 shows the transects of the 73 identified PMC front structures as a function of albedo and distance from the front. The transects are separated based on available near-coincident SABER temperature profiles (see Section 2.2). In the mostly clear region, the sharp drop off from the bright cloud boundary is apparent. The albedo values are generally less than 10×10^{-6} sr^{-1} within 200 km of the sharp boundary. In contrast, there is a large variability in albedo in the cloudy region. The mean albedo ±1 standard deviation and median albedo at the peak boundary are $26.1 \pm 12.6 \times 10^{-6}$ sr^{-1} and 21.9×10^{-6} sr^{-1}, respectively. Approximately 100 km from the peak albedo, the mean albedo decreases to $2.4 \pm 2.2 \times 10^{-6}$ sr^{-1} in the mostly clear region and $14.0 \pm 9.1 \times 10^{-6}$ sr^{-1} in the cloudy region.

2.2. TIMED/SABER Temperatures

SABER is a limb-scanning infrared radiometer on the Thermosphere Ionosphere Mesosphere Energetics and Dynamics (TIMED) satellite. Among other variables, SABER measures global temperature and water vapor from ~10 to 110 km (Esplin et al., 2023; Russell et al., 1999). While continuous measurements over the latitude range of 50°N–50°S are available since 2002, high-latitude SABER measurements in both hemispheres are limited to only a part (~2 months) of the PMC season due to yaw maneuvers in the TIMED satellite. In the NH, these measurements are limited to the first part of the PMC season. NH high-latitude coverage in summer has been shifting progressively earlier with each year and is available, for example, from 20 May to 15 July in 2007 and from 23 April to 19 June in 2022. We use SABER Level 2A version 2.07 data from 2007 to 2019 and version 2.08 data from 2020 to 2022 in this study. Version 2.08 reprocessed data is available from 15 December 2019.

Near-coincident SABER temperature and water vapor measurements are identified within ±5° latitude, ±20° longitude, and ±90 min of a PMC front structure observed by CIPS. For a given PMC front, if two SABER profiles satisfy these criteria, only the nearest profile in the mostly clear region is considered. Inversion layers are detected as temperature perturbations from the near-coincident temperature profiles at PMC altitudes from 80 to 90 km. Single temperature profile random errors are 1.8 K at 80 km and 3.6 K at 90 km. The vertical resolution is 2 km, but these profiles are reported at a spacing of 0.4 km. For a temperature inversion to be detected, the local maximum or peak temperature must occur between 80 and 90 km and must be below the mesopause if the mesopause occurs below 90 km. Note that we do not refer to these temperature inversions as MILs, as the conservative definition requires that MILs are layers of enhanced temperature ~10 km deep with amplitudes greater than ~10 K that extend over thousands of kilometers and over several days (e.g., Mariaccia et al., 2023; Meriwether & Gardner, 2000). SABER temperature profiles used in this study are instantaneous measurements. Although consecutive profiles can provide us a measure of the horizontal extent of the temperature inversion layer, the narrow PMC altitudes between 80 and 90 km constrain us to consider inversion layers with widths less than 10 km.

As in an MIL, we characterize a temperature inversion by its amplitude, temperature lapse rate above the inversion layer peak (topside lapse rate), and the temperature gradient below the inversion layer peak (bottomside

gradient). The temperature inversion amplitude is defined as the temperature difference between the local maximum at the temperature peak and local minimum below the peak. The topside temperature lapse rate is calculated using a linear fit between the temperature maximum and the first 5 km (or lower if the mesopause occurs within these 5 km) above the maximum. The bottomside temperature gradient is calculated using a linear fit between the temperature minimum at the bottom of the inversion layer and the maximum at the temperature peak. The temperature gradient is calculated as the change in temperature (∂T) with change in altitude (∂Z). The lapse rate is the negative of $\partial T/\partial Z$. Thus, the overall decrease in temperature with increase in altitude in the mesosphere implies a positive lapse rate, and for a temperature inversion layer, both the bottomside temperature gradient and the topside temperature lapse rate are, by definition, positive.

SABER near-coincident temperature measurements occur for 24 out of the 73 PMC fronts and are identified in the years 2007–2015. Temperature inversions are found between 80 and 90 km in all 24 measurements. Figure 2 shows CIPS cloud albedo along the transects across the 24 PMC front structures in the vicinity of the SABER near-coincident temperature measurements (black lines) as well as the albedo along the 49 other transects (gray lines). For the 24 transects, the mean albedo $\pm$1 standard deviation and the median albedo (not shown) at the peak boundary are $22.8 \pm 11.2 \times 10^{-6}$ sr^{-1} and 19.8×10^{-6} sr^{-1}, respectively. Approximately 100 km from the peak albedo, the mean albedo decreases to $1.7 \pm 1.6 \times 10^{-6}$ sr^{-1} in the mostly clear region and $12.0 \pm 6.8 \times 10^{-6}$ sr^{-1} in the cloudy region.

3. Results

3.1. Characteristics of PMC Fronts

The 73 front structures were identified in June and July of all available PMC seasons (as noted in Section 2.2 no CIPS data are available in the NH 2017 PMC season). The cross-track orientation of the PMC images in the 2018 PMC season, which resulted in gaps between successive images along the orbit track, may be a factor in the lower number of fronts identified in that season. The lengths of the 73 fronts vary from ~250 km to greater than 900 km, and no obvious trailing waves are detected. The actual length of longer fronts are limited by the CIPS orbit swath size. Since fronts can be identified only when clouds are abundant, the latitude range for their occurrence is constrained to latitudes of ~65°N–85°N.

Figure 3a shows that these structures occur at all longitudes and poleward of 60°N. The total numbers of front structures per year and in each 30° longitude bin for all years are enumerated in the tables in Figure 3. More fronts ($\geq$10) are identified in years 2007, 2011, and 2012, and between longitudes 150°E and 180°E. The fronts also appear to be distributed in the pattern of an oval that is oriented with its long axis approximately along the line from 150°E to 330°E. Given that the occurrence of fronts depends on cloud abundance, we examined whether identification of more fronts truly implies that more fronts occurred or whether CIPS just observed more fronts because it detected more clouds. Figures 3b and 3c show the number of fronts relative to the average cloud frequency observed in June and July of each year and in each longitude bin, respectively. This is shown as the ratio of the number of fronts to the average cloud occurrence frequency. Cloud frequency is calculated as the percentage ratio of the total number of cloud observations to the total number of observations at all longitudes between 65 and 85°N. The peaks in Figures 3b and 3c suggest that more fronts did occur in years 2007, 2011, and 2012, and from longitudes 150°E–180°E, irrespective of cloud frequency. The reason for the apparent oval pattern and the increase in number of fronts in certain years and from longitudes 150°E–180°E is unclear.

We also analyzed if the cloudy region near the front had significantly higher cloud albedo than average, which made it easier to detect the fronts. We compared the average albedo along ~150 km of the transects in the cloudy region (not including the bright boundary itself and the mostly clear region) to the zonal mean average albedo over the latitude range spanned by the ~150 km transect. The zonal mean was calculated for all orbits in all years, within $\pm$2 days of the day-of-year on which the front was found. In general, the overall transect albedo values are similar to the values of the larger dataset, giving us confidence that albedos in the cloudy region are typically not higher than the average and do not bias the visual front detection.

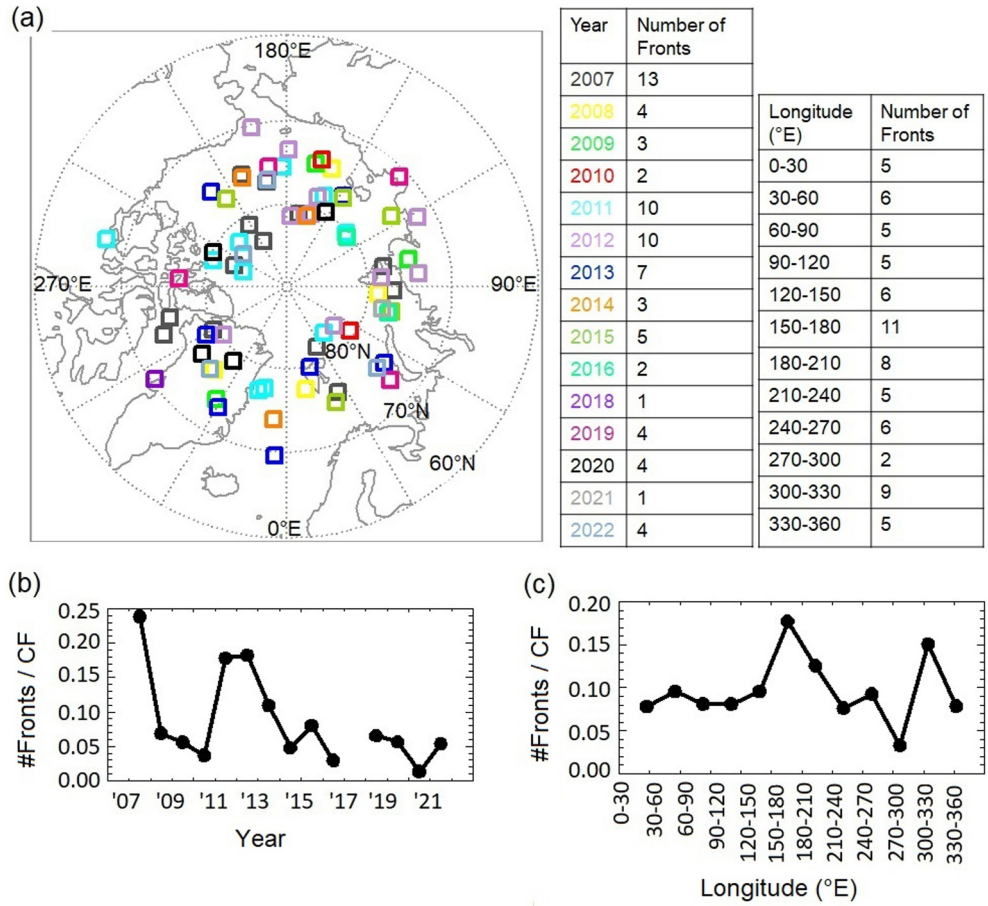

Year	Number of Fronts
2007	13
2008	4
2009	3
2010	2
2011	10
2012	10
2013	7
2014	3
2015	5
2016	2
2018	1
2019	4
2020	4
2021	1
2022	4

Longitude (°E)	Number of Fronts
0-30	5
30-60	6
60-90	5
90-120	5
120-150	6
150-180	11
180-210	8
210-240	5
240-270	6
270-300	2
300-330	9
330-360	5

Figure 3. (a) Location of front structures observed in the NH 2007–2022 PMC seasons. The tables list the number of fronts per year and in 30° longitude bins. (b) The ratio of the number of fronts to the average cloud frequency (CF) per year. (c) The ratio of the number of fronts to the average CF per longitude bin in all years.

3.2. Influence of Temperature Inversions on PMC Front Formation

3.2.1. Case Study

An example of a PMC front observed by CIPS on 21 June 2011 (orbit start time or start of data collection is 23:44 UT on 20 June 2011) and the locations of the near-coincident and neighboring SABER measurements are shown on an NH polar map in Figure 4. The SABER measurements are given in terms of event number. Note that in the SABER data, for a given orbit, each retrieved profile (function of pressure, altitude, zenith angle, latitude, longitude, and time) is assigned an event number. The PMC front is identified in CIPS orbit 22625 at 00:10 UT on 21 June 2011 from ~230 to 270°E and centered at ~80°N. In SABER orbit 51640 on 21 June 2011, near-coincident event E27 (01:32:53 UT, 77.1°N, 259.8°E) was observed in the mostly clear region ~82 min after the CIPS observation. Event E26 (01:32:11 UT, 79.1°N, 266.4°E) was observed at the edge of the front, also ~82 min after the CIPS observation. Earlier events E24 (01:30:16 UT, 82.9°N, 302.6°E) and E25 (01:31:01 UT, 81.9°N, 284.5°E) were observed west of the front within 1 min of each other at progressively increasing latitudes and longitudes. While data from E28 is not available, E29 (01:35:04 UT, 70.2°N, 248.7°E) was observed south and east of the front outside the CIPS observation area.

Figure 5a shows the temperature profiles for events E24-E27 and E29 from 70 to 95 km. The temperatures averaged over 80–90 km for events E24-E27 and E29 are 140.2, 137.6, 146.4, 146.6, and 142.1 K, respectively. Temperature inversions in the PMC altitude region from 80 to 90 km are present in all profiles, and their locations are designated by labels L1-L7. In this study, we consider a temperature inversion to be significant if the amplitude is greater than 4 K (SABER temperature random errors are 1.8 K at 80 km and 3.6 K at 90 km). Based

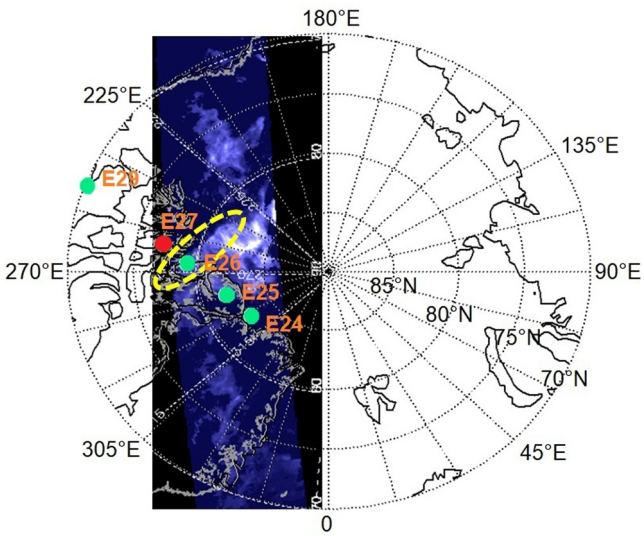

Figure 4. PMC front observed by CIPS on 21 June 2011 and SABER near-coincident (red dot) and neighboring events (green dots).

on this amplitude threshold, the inversion layers L1 in event E24 and L3 in E25 are not considered inversion layers. The characteristics of the five significant temperature inversions are summarized in Table 1.

Both temperature (T) and water vapor (H_2O) contribute to PMC formation (e.g., Dalin et al., 2011). PMCs form under conditions of low temperatures (generally $T < 145$ K) and enhanced water vapor (generally $H_2O > 1.0$ ppmv) (e.g., Rong et al., 2012) when the saturation ratio (S) is much greater than one (i.e., supersaturated state). S is defined as the ratio of water vapor partial pressure (P_{H2O}) to saturation vapor pressure (P_{SAT}). From Murphy and Koop (2005), for a temperature T, P_{SAT} is defined as

$$\log(P_{SAT}) = 9.550426 - \frac{5723.265}{T} + 3.53068\log T - 0.007238232T \quad (1)$$

P_{H2O} is the water vapor multiplied by the pressure at that altitude. From Table 1, the saturation ratio averaged over 80–90 km is 5.5 for E24 and >20 for E25-27 and E29. The albedos averaged over the 2° latitude × 2° longitude bin around the SABER measurements indicate that the albedo values are mostly consistent with the saturation ratio values (i.e., clouds form only when $S >> 1$). Inconsistencies between S and albedo (e.g., if $S >> 1$ but no clouds are observed) could be due to a combination of SABER along-track observations that span an average of ∼2° (∼200 km) and movement of the PMC front. For example, Thurairajah et al. (2021) have suggested that PMC fronts can move at a speed of ∼60 m/s in the northwest direction.

Figure 5b shows the squared buoyancy frequency (N^2) calculated from the corresponding temperature profiles. N^2 is given by

$$N^2 = \frac{g}{T}\left(\frac{\partial T}{\partial z} + \Gamma_d\right) \quad (2)$$

where g is the gravitational constant, z is the altitude, and Γ_d is the adiabatic lapse rate. A positive N^2 indicates a stable region while a negative N^2 indicates an unstable region. While all events show stable and unstable regions from 80 to 90 km, for events E26 and E27, the high N^2 at ∼85 and ∼82 km, respectively, surrounded by low-stability or unstable regions, along with the presence of significant inversion layers, present favorable conditions for horizontal wave propagation. The inversion layers in adjacent profiles E26 and E27 extend over 260 km horizontally, but over different altitudes; minimum and maximum temperatures occur between 83.8 and 85.8 km for E26 and between 80.2 and 82.4 k for E27. Temperature inversion layers are also present in SABER temperature profiles on 20 June 2011 (E27, 01:16 UT, 79.1°N, 273.2°E, amplitude = 9.2 K) and on 22 June 2011 (E27, 01:47 UT, 79.3°N, 260.2°E, amplitude = 24 K). The large amplitudes (>12 K), horizontal spans, and persistence over multiple days suggest that these perturbations may be characterized as MILs. We propose that the inversion layers in E27 (L5) and E26 (L4) may have formed a thermal duct that supported wave propagation. However, the higher temperatures (Tpeak = 173.8 K) associated with E27 (L5) destroyed clouds, whereas the relatively lower temperatures (Tpeak = 153.1 K) associated with E26 (L4) may have supported the formation of the solitary wave or PMC front identified in Figure 4. The inversion layers in E24 (L1) and E25 (L3) were not significant enough to have supported horizontal wave propagation, and there are not enough clouds for the formation of a PMC front in E24 (L2). No CIPS PMC data is available near E29.

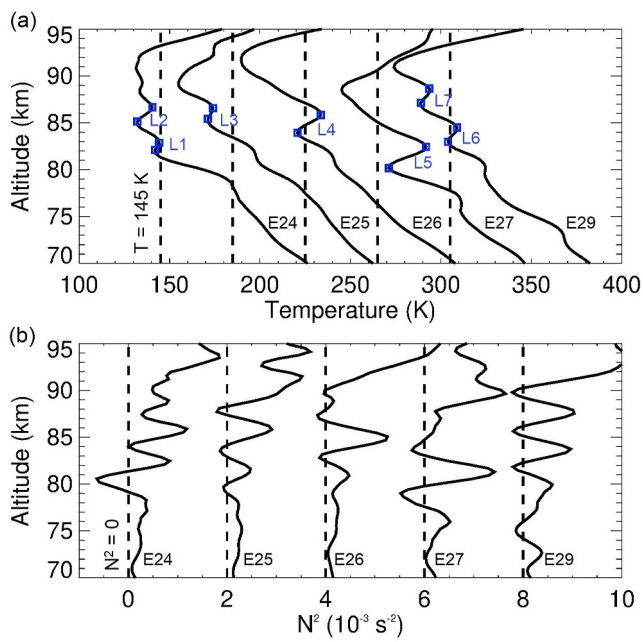

Figure 5. (a) SABER temperature profiles for events E24-E27 and E29. Temperature profiles E25-E27 and E29 are offset by 40 K for clarity. L1-L7 denote inversion layers from 80 to 90 km. Blue squares indicate the local maximum at the inversion layer peak and local minimum below the peak. (b) Squared buoyancy frequency (N^2) for SABER events E24-E27, and E29. N^2 profiles E25-E27 and E29 are offset by 2×10^{-3} s^{-2}. Dashed lines in (a) indicate T = 145 (K) and in (b) indicate $N^2 = 0$.

Table 1
Characteristics of SABER Temperatures in Orbit 51640 and CIPS Albedo in Orbit 22625

SABER event	E24		E25	E26	E27	E29	
$T_{80–90\ km}$ (K)	140.2		137.6	146.4	146.6	142.1	
$S_{80–90\ km}$	5.5		313.5	34.5	22.4	27.4	
Albedo (10^{-6} sr^{-1})	0.9		3.9	6.9	1.7	n/a	
Inversion Layer	L1[a]	L2	L3[a]	L4	L5	L6	L7
Z_{peak} (km)		86.7		86.2	82.5	84.5	88.3
T_{peak} (K)		140.5		153.1	171.8	148.9	133.8
Amplitude (K)		8.3		12.4	16.0	5.0	4.8
Topside lapse rate (K/km)		3.6		10.0	11.1	9.7	6.9
Bottomside gradient (K/km)		4.4		5.4	6.0	3.1	5.3

[a]Inversion layer is not significant.

3.2.2. Characteristics of Near-Coincident Temperature Inversions

As noted above, temperature inversion layers between 80 and 90 km occur in all 24 near-coincident SABER temperature measurements. Six out of the 24 temperature profiles indicate the presence of double temperature inversions. Thus, the total number of inversion layers identified is 30. In the case of MILs, double layers are a common occurrence (Meriwether & Gardner, 2000). The MILs that form between 65 and 85 km are known as 'lower' MILs. These lower MILs form due to breaking PWs and GWs (e.g., Salby et al., 2002). The MILs that form between 85 and 100 km are referred to as 'upper' MILs and are known to be driven by GW breaking, wave-wave interactions, and/or chemical heating (e.g., Meriwether & Gardner, 2000). In this study, since we analyze inversion layers in a narrow altitude region (80–90 km), we do not categorize these temperature inversions as lower or upper inversion layers. We also note the monthly zonal mean occurrence rate of temperature inversions in the high-latitude summer (>65°N), from 80 to 90 km and with amplitudes >4 K, is ∼20% (not shown). These inversion layers are thus not ubiquitous features.

Figure 6a shows the 24 SABER temperature profiles that are in near coincidence with PMC fronts identified in CIPS data. The temperature inversion peaks from 80 to 90 km are denoted by the squares and the red dashed line indicates 145 K. There are five inversion layers with peak temperature less than 145 K. The lowest temperature is 135.2 K at 86.1 km on 6 July 2007. This inversion layer is one of the double temperature inversions. The second inversion layer peak on 6 July 2007 is at 81.9 km with a peak temperature of 157.3 K. The highest peak temperature is 171.8 K at 82.5 km on 20 June 2011 (see also Figure 5a). The location of the SABER profiles are distributed across the front locations, with five profiles located in the cloudy region, six profiles at the edge of the front, and 13 profiles in the mostly clear region. Given the likely movement of the front, our near-coincident criteria and the PMC altitude can vary from ∼80 to 90 km, the temperatures and saturation profiles (not shown) do not necessarily agree with the CIPS observations of cloudy and mostly clear regions. Here, we assume that the presence of temperature inversions coincided with mesospheric conditions conducive to supporting the formation of PMCs ($S >> 1$).

Numerical simulations of GW propagation in thermal ducts (Dong et al., 2018) have shown that when a wave packet enters the duct area there is an initial increase in wave amplitude followed by a reduction in amplitude due to dispersion and energy leakage. In our case, the initial increase in GW amplitude would likely destroy clouds, leading to a sharp boundary between cloudy and mostly clear regions. For ground- or space-based observations, the horizontal propagation of ducted GWs can manifest as a quasi-monochromatic wave or can appear as trailing wave crests that decrease in amplitude as they propagate inside the duct and dissipate. Assuming that the temperature and water vapor in the cold troughs of gravity waves are conducive to the formation of PMCs, we would see a region of bright cloud in the first wave trough followed by trailing wave signatures in the cloudy regions with decreasing cloud brightness as the wave amplitude decreases. The study by Dalin et al. (2013) showed an NLC front or a solitary wave modulated by two closely spaced 'long wavy bands', and followed by several small scale GWs with horizontal wavelengths of 9–12 km. However, the visually inspected CIPS PMC images do not show any apparent trailing waves. It is not clear if only quasi-monochromatic waves are observed or if the CIPS

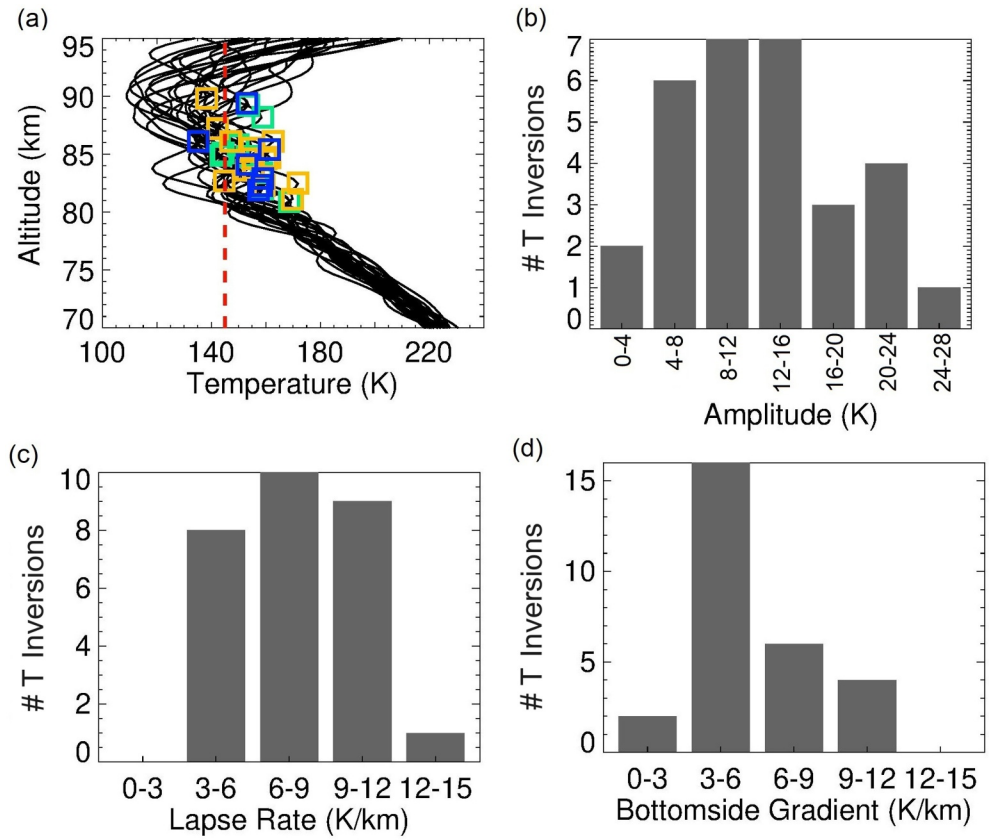

Figure 6. (a) SABER temperature profiles for measurements in near-coincidence with fronts identified in CIPS data. Red vertical dashed line indicates $T = 145$ (K). Squares show the peak temperature of the temperature inversions, with blue, orange, and green indicating the profiles located in the cloudy region, mostly clear region, and edge of the front, respectively. (b) Histogram of the amplitudes of the temperature inversions shown in (a). (c) Histogram of significant temperature inversions topside lapse rate. (d) Histogram of significant temperature inversions bottomside gradient.

resolution is too coarse to capture the trailing waves. Moreover, in a recent study by Ramachandran et al. (2023), a series of direct numerical simulations by a 2D model showed that the width of the thermal duct had a substantial effect on the morphology of a mesospheric bore. For example, in a narrow duct, the bore formed faster and was followed by fewer trailing waves. Thus, the narrow region of the SABER near-coincident temperature inversion layers might have played a role in constraining any trailing waves.

Figures 6b–6d show histograms of temperature inversion layer characteristics of amplitude, topside lapse rate, and bottomside gradient from the 24 temperature profiles. Overall, the temperature inversion amplitude varies from 1.1 K (not significant) to 26.1 K with a mean of 12.1 K. For the histogram in Figure 6b, the amplitudes are binned in 4 K bins, which shows that the most prevalent amplitudes are between 8 and 20 K. Only two temperature inversions have amplitudes less than 4 K and are considered not significant; the inversion layer amplitude on 28 June 2007 is 1.1 K and the amplitude on 6 July 2007 is 3.4 K. This temperature inversion on 6 July 2007 is one of the double inversion layers identified with the lowest peak temperature of 135.2 K, as noted previously. Thus, out of the 24 near-coincident temperature profiles, 23 profiles have significant temperature inversions for a total of 28 significant temperature inversions with an average amplitude of 12.8 K. Note that there are 15 temperature inversions with amplitudes >12 K. SABER observations indicate that adjacent temperature profiles also have inversion layers but with amplitudes reduced by ∼50% or less. Given that the horizontal distances between adjacent SABER profiles vary from ∼260 to 560 km, some of these inversion layers may be considered MILs solely based on their extent over large distances. However, the lifetime of these inversion layers is not clear. There are not many studies of daily MIL occurrence at high-latitude PMC altitudes in the summer for comparison purposes. However, these temperature inversion amplitudes are only slightly higher than the MIL amplitudes

reported by Ardalan et al. (2022) at a midlatitude location in France (44° N, 6° E) in summer. That lidar study noted lower MIL (~50–75 km) amplitudes between 5 and 20 K.

Figures 6c and 6d show the histograms of the topside lapse rate and bottomside gradient for the 28 significant inversion layers. The topside lapse rate has a peak of 6–9 K/km and average of 7.8 K/km. The bottomside gradient has a skewed distribution with a peak of 3–6 K/km and average of 6.1 K/km. The positive bottomside temperature gradient is a favorable region for GW breaking and can also lead to dynamical instabilities and the generation of secondary GWs (Hauchecorne et al., 1987). A positive topside lapse rate implies a reduction in atmospheric stability and that the atmosphere may become convectively unstable. The adiabatic lapse rate of the mesosphere is 9.5 K/km. A topside lapse rate close to the adiabatic lapse rate indicates wave saturation and convective instability (e.g., Lübken et al., 2006; Whiteway & Carswell, 1995). If the lapse rate was greater than the adiabatic lapse rate, convective instability due to wave forcing would return the lapse rate to the adiabatic lapse rate (Fritts et al., 2018). The distribution of lapse rates in Figure 6c indicates both stable regions (i.e., topside lapse rate <9.5 K/km) and unstable regions above the inversion layers.

4. Summary and Conclusion

PMC front structures are defined by a sharp boundary that separates mesospheric cloudy and mostly clear regions with the clouds at the boundary brighter than the adjacent cloudy region. Using CIPS PMC albedo images from the NH 2007–2022 PMC seasons, 73 PMC fronts were identified. Given that the methodology to identify fronts is based on an initial visual identification, this is likely a small subset but robust representation of the larger front population. These 73 fronts are located at all longitudes, with lengths varying from 250 km to >900 km. SABER near-coincident temperature profiles occurred for 24 out of the 73 front structures. All 24 temperature profiles are characterized by temperature inversions between 80 and 90 km, the PMC altitude region. Moreover, buoyancy frequencies calculated from these temperature profiles indicate an unstable region surrounded by a stable region (not shown), thus facilitating wave propagation into a thermal duct created by the inversion layer.

MILs can form by a variety of mechanisms including GW dissipation. Previous studies have shown that MILs can form as a response to GWs that attain large amplitudes and cause strong wind shears and large variations in local static stability. This is also a formation mechanism of mesospheric bores. The near-coincident temperature inversions were identified from instantaneous SABER observations. Thus, these perturbations are not necessarily large-scale long-lasting MILs and may have formed due to GWs, tides and/or PWs. However, adjacent temperature profiles indicate that large-amplitude (>12 K) temperature inversions are persistent over distances of at least 260–560 km and could be large-scale features that may be characterized as MILs. We propose that temperature inversions identified in all 24 of the SABER profiles that were nearly coincident with the PMC fronts suggest that some of the inversion layers may be responsible for the sharp boundary that separates cloudy and mostly clear regions. Based on the structure of the squared buoyancy frequency, thermal ducts formed by the inversion layer—potential MILs—may have supported horizontal GW propagation and the formation of PMC fronts. Coincident wind observations and model simulations may provide future insight into this formation mechanism.

Data Availability Statement

CIPS Level 2, version 5.20, and revision 05 data can be downloaded from https://spdf.gsfc.nasa.gov/pub/data/aim/cips/data/ (CIPS, 2023). SABER Level 2A, version 2.07, and version 2.08 data can be downloaded from the SABER/TIMED mission science website at http://saber.gats-inc.com (SABER, 2023). All websites are in English.

Acknowledgments
This work was supported by NSF AGS award 2149483. The AIM mission is supported by the NASA Small Explorer Contract NAS5-03132. BT thanks graduate student Sarvesh Patil for calculating the monthly frequency of the temperature inversions. CYC was supported by NASA award 80NSSC22K0726.

References

Ardalan, M., Keckhut, P., Hauchecorne, A., Wing, R., Meftah, M., & Farhani, G. (2022). Updated Climatology of Mesospheric Temperature Inversions Detected by Rayleigh Lidar above Observatoire de Haute Provence. France, Using a K-Mean Clustering Technique. *Atmosphere*, *13*(5), 814. https://doi.org/10.3390/atmos13050814

Bailey, S. M., Thomas, G. E., Rusch, D. W., Merkel, A. W., Jeppesen, C. D., Carstens, J. N., et al. (2009). Phase functions of polar mesospheric cloud ice as observed by the CIPS instrument on the AIM satellite. *Journal of Atmospheric and Solar-Terrestrial Physics*, *71*(3–4), 373–380. https://doi.org/10.1016/j.jastp.2008.09.039

Benze, S., Randall, C. E., DeLand, M. T., Thomas, G. E., Bailey, S. M., Russell, J. M., III, & Merkel, A. W. (2011). Evaluation of AIM CIPS measurements of polar mesospheric clouds by comparison with SBUV data. *Journal of Atmospheric and Solar-Terrestrial Physics*, *73*(14–15), 2065–2072. https://doi.org/10.1016/j.jastp.2011.02.003

Benze, S., Randall, C. E., DeLand, M. T., Thomas, G. E., Rusch, D. W., Bailey, S. M., et al. (2009). Comparison of polar mesospheric cloud measurements from the Cloud Imaging and Particle Size experiment and the solar backscatter ultraviolet instrument in 2007. *Journal of Atmospheric and Solar-Terrestrial Physics*, *71*(3–4), 365–372. https://doi.org/10.1016/j.jastp.2008.07.014

Carstens, J. N., Bailey, S. M., Lumpe, J. D., & Randall, C. E. (2013). Understanding uncertainties in the retrieval of polar mesospheric clouds from the cloud imaging and particle size experiment in the presence of a bright Rayleigh background. *Journal of Atmospheric and Solar-Terrestrial Physics*, *104*, 197–212. https://doi.org/10.1016/j.jastp.2013.08.006

Chandran, A., Rusch, D. W., Palo, S. E., Thomas, G. E., & Taylor, M. J. (2009). Gravity wave observations in the summertime polar mesosphere from the cloud imaging and particle size (CIPS) experiment on the AIM spacecraft. *Journal of Atmospheric and Solar-Terrestrial Physics*, *71*(3–4), 392–400. https://doi.org/10.1016/j.jastp.2008.09.041

CIPS. (2023). The cloud imaging and particle size experiment data (level 2, version 05.20, revision 05). [Dataset] Retrieved from https://spdf.gsfc.nasa.gov/pub/data/aim/cips/data/

Dalin, P., Connors, M., Schofield, I., Dubietis, A., Pertsev, N., Perminov, V., et al. (2013). First common volume ground-based and space-based measurements of the mesospheric front in noctilucent clouds. *Geophysics Research Letters*, *40*, 1–6. https://doi.org/10.1002/2013GL058553

Dalin, P., Kirkwood, S., Moström, A., Stebel, K., Hoffmann, P., & Singer, W. (2004). A case study of gravity waves in noctilucent clouds. *Annales Geophysicae*, *22*(6), 1875–1884. https://doi.org/10.5194/angeo-22-1875-2004

Dalin, P., Pertsev, N., Dubietis, A., Zalcik, M., Zadorozhny, A., Connors, M., et al. (2011). A comparison between ground-based observations of noctilucent clouds and Aura satellite data. *Journal of Atmospheric and Solar-Terrestrial Physics*, *73*(14–15), 2097–2109. https://doi.org/10.1016/j.jastp.2011.01.020

Dewan, E., & Picard, R. (1998). Mesospheric bores. *Journal of Geophysical Research*, *103*(D6), 6295–6305. https://doi.org/10.1029/97jd02498

Dewan, E., & Picard, R. (2001). On the origin of mesospheric bores. *Journal of Geophysical*, *106*(D3), 2921–2927. https://doi.org/10.1029/2000jd900697

Dong, W., Fritts, D. C., Thomas, G. E., & Lund, T. S. (2021). Modeling responses of polar mesospheric clouds to gravity wave and instability dynamics and induced large-scale motions. *Journal of Geophysical Research: Atmospheres*, *126*(13), e2021JD034643. https://doi.org/10.1029/2021JD034643

Dong, W., Zhang, S., Huang, C., Huang, K., Gong, Y., & Gan, Q. (2018). A numerical study of gravity wave propagation characteristics in the stratospheric thermal duct. *Journal of Geophysical Research: Atmospheres*, *123*(21), 11918–11937. https://doi.org/10.1029/2018JD029190

Dubietis, A., Dalin, P., Balčiūnas, R., Černis, K., Pertsev, N., Sukhodoev, V., et al. (2011). Noctilucent clouds: Modern ground-based photographic observations by a digital camera network. *Applied Optics*, *50*(28), F72–F79. https://doi.org/10.1364/AO.50.000F72

Esplin, R., Mlynczak, M. G., Russell, J. M., & Gordley, L. L., & The SABER Team. (2023). Sounding of the atmosphere using Broadband emission Radiometry (SABER): Instrument and science measurement description. *Earth and Space Science*, *10*(9), e2023EA002999. https://doi.org/10.1029/2023EA002999

France, J. A., Harvey, V. L., Randall, C. E., Collins, R. L., Smith, A. K., Peck, E. D., & X. Fang, X. (2015). A climatology of planetary wave-driven mesospheric inversion layers in the extratropical winter. *Journal of Geophysical Research: Atmospheres*, *120*(2), 399–413. https://doi.org/10.1002/2014JD022244

Fritts, D. C., Kaifler, N., Kaifler, B., Geach, C., Kjellstrand, C. B., Williams, B. P., et al. (2020). Mesospheric bore evolution and instability dynamics observed in PMC Turbo imaging and Rayleigh Lidar profiling over Northeastern Canada on 13 July 2018. *Journal of Geophysical Research: Atmospheres*, *125*(14), e2019JD032037. https://doi.org/10.1029/2019JD032037

Fritts, D. C., Laughman, B., Wang, L., Lund, T. S., & Collins, R. L. (2018). Gravity wave dynamics in a mesospheric inversion layer: 1. Reflection, trapping, and instability dynamics. *Journal of Geophysical Research: Atmospheres*, *123*(2), 626–648. https://doi.org/10.1002/2017JD027440

Gadsden, M., & Parviainen, P. (1996). Observing noctilucent clouds. *International Association of Geomagnetism and Aeronomy*. available on http://www.iug-g.org/IAGA/iaga_pages/pdf/ONC_sep06.pdf

Gan, Q., Zhang, S. D., & Yi, F. (2012). TIMED/SABER observations of lower mesospheric inversion layers at low and middle latitudes. *Journal of Geophysical Research*, *117*(D7), D07109. https://doi.org/10.1029/2012JD017455

Hauchecorne, A., Chanin, M. L., & Wilson, R. (1987). Mesospheric temperature inversion and gravity wave breaking. *Geophysical Research Letters*, *14*(9), 933–936. https://doi.org/10.1029/gl014i009p00933

Hervig, M. E., Siskind, D. E., Stevens, M. H., & Deaver, L. E. (2013). Inter-hemispheric comparison of PMCs and their environment from SOFIE observations. *Journal of Atmospheric and Solar-Terrestrial Physics*, *104*, 285–298. https://doi.org/10.1016/j.jastp.2012.10.013

Hozumi, Y., Saito, A., Sakanoi, T., Yamazaki, A., Hosokawa, K., & Nakamura, T. (2019). Geographical and seasonal variability of mesospheric bores observed from the International Space Station. *Journal of Geophysical Research: Space Physics*, *124*(5), 3775–3785. https://doi.org/10.1029/2019JA026635

Irving, B. K., Collins, R. L., Lieberman, R. S., Thurairajah, B., & Mizutani, K. (2014). Mesospheric inversion layers at chatanika, Alaska (65°N, 147°W): Rayleigh lidar observations and analysis. *Journal of Geophysical Research: Atmospheres*, *119*(19), 11235–11249. https://doi.org/10.1002/2014JD021838

Karlsson, B., Randall, C. E., Benze, S., Mills, M., Harvey, V. L., Bailey, S. M., & Russell III, J. M. (2009). Intra-seasonal variability of polar mesospheric clouds due to inter-hemispheric coupling. *Geophysical Research Letters*, *36*(20), L20802. https://doi.org/10.1029/2009GL040348

Liu, H.-L., Hagan, M. E., & Roble, R. G. (2000). Local mean state changes due to gravity wave breaking modulated by the diurnal tide. *Journal of Geophysical Research*, *105*(D10), 12381–12396. https://doi.org/10.1029/1999JD901163

Lübken, F.-J., Strelnikov, B., Rapp, M., Singer, W., Latteck, R., Brattli, A., et al. (2006). The thermal and dynamical state of the atmosphere during polar mesosphere winter echoes. *Atmospheric Chemistry and Physics*, *6*(1), 13–24. https://doi.org/10.5194/acp-6-13-2006

Lumpe, J. D., Bailey, S. M., Carstens, J. N., Randall, C., Rusch, D., Thomas, G., et al. (2013). Retrieval of polar mesospheric cloud properties from CIPS: Algorithm description, error analysis and cloud detection sensitivity. *Journal of Atmospheric and Solar-Terrestrial Physics*, *104*, 167–196. https://doi.org/10.1016/j.jastp.2013.06.007

Mariaccia, A., Keckhut, P., Hauchecorne, A., Khaykin, S., & Ratynski, M. (2023). Co-located wind and temperature observations at mid-latitudes during mesospheric inversion layer events. *Geophysical Research Letters*, *50*(9), e2022GL102683. https://doi.org/10.1029/2022GL102683

McClintock, W., Rusch, D. W., Thomas, G. E., Merkel, A., Lankton, M., Drake, V., et al. (2009). The cloud imaging and particle size experiment on the aeronomy of ice in the mesosphere mission: Instrument concept, design, calibration, and on-orbit performance. *Journal of Atmospheric and Solar-Terrestrial Physics*, *71*(3–4), 340–355. https://doi.org/10.1016/j.jastp.2008.10.011

Megner, L., Stegman, J., Pautet, P.-D., & Taylor, M. J. (2018). First observed temporal development of a noctilucent cloud ice void. *Geophysical Research Letters*, *45*(18), 10003–10010. https://doi.org/10.1029/2018GL078501

Meriwether, J. W., & Gardner, C. S. (2000). A review of the mesosphere inversion layer phenomenon. *Journal of Geophysical Research*, *105*(D10), 12405–12416. https://doi.org/10.1029/2000JD900163

Meriwether, J. W., & Gerrard, A. J. (2004). Mesosphere inversion layers and stratosphere temperature enhancements. *Reviews of Geophysics*, *42*, RG3003. https://doi.org/10.1029/2003RG000133

Meriwether, J. W., & Mlynczak, M. G. (1995). Is chemical heating a major cause of the mesosphere inversion layer? *Journal of Geophysical Research*, *100*(D1), 1379–1387. https://doi.org/10.1029/94JD01736

Murphy, D. M., & Koop, T. (2005). Review of the vapour pressures of ice and supercooled water for atmospheric applications. *Quarterly Journal of the Royal Meteorological Society*, *131*(608), 1539–1565. https://doi.org/10.1256/qj.04.94

Oberheide, J., Liu, H.-L., Gusev, O. A., & Offermann, D. (2006). Mesospheric surf zone and temperature inversion layers in early November 1994. *Journal of Atmospheric and Solar-Terrestrial Physics*, *68*(15), 1751–1763. https://doi.org/10.1016/j.jastp.2005.11.013

Pautet, P.-D., Taylor, M. J., Snively, J. B., & Solorio, C. (2018). Unexpected occurrence of mesospheric frontal gravity wave events over South Pole (90°S). *Journal of Geophysical Research: Atmospheres*, *123*(1), 160–173. https://doi.org/10.1002/2017JD027046

Ramachandran, K., Sivakandan, M., Chau, J. L., Urco, J. M., Gerding, M., Grundmann, S., & Smith, S. M. (2023). Investigation of a dissipating mesospheric bore using airglow imager and direct numerical simulation. *Journal of Geophysical Research: Space Physics*, *128*(4), e2022JA031114. https://doi.org/10.1029/2022JA031114

Ramesh, K., Sridharan, S., & Vijaya Bhaskara Rao, S. (2014). Causative mechanisms for the occurrence of a triple layered mesospheric inversion event over low latitudes. *Journal of Geophysical Research: Space Physics*, *119*(5), 3930–3943. https://doi.org/10.1002/2013ja019750

Rong, P. P., Russell, J. M., III, Hervig, M. E., & Bailey, S. M. (2012). The roles of temperature and water vapor at different stages of the polar mesospheric cloud season. *Journal of Geophysical Research*, *117*(D4), D04208. https://doi.org/10.1029/2011JD016464

Rusch, D. W., Thomas, G. E., McClintock, W., Merkel, A. W., Bailey, S. M., Russell, J. M., III, et al. (2009). The cloud imaging and particle size experiment on the aeronomy of ice in the mesosphere mission: Cloud morphology for the northern 2007 season. *Journal of Atmospheric and Solar-Terrestrial Physics*, *71*(3–4), 356–364. https://doi.org/10.1016/j.jastp.2008.11.005

Russell, J. M., III, Bailey, S. M., Gordley, L. L., Rusch, D. W., Horányi, M., Hervig, M. E., et al. (2009). Aeronomy of ice in the mesosphere (AIM): Overview and early science results. *Journal of Atmospheric and Solar-Terrestrial Physics*, *71*(3–4), 289–299. https://doi.org/10.1016/j.jastp.2008.08.011

Russell, J. M., III, Mlynczak, M. G., Gordley, L. L., Tansock, J., & Esplin, R. (1999). An overview of the SABER experiment and preliminary calibration results. *Proceedings of the SPIE, 44th Annual Meeting*, *3756*, 277–288. Denver, Colorado, USA, 18–23 July 1999.

Russell, J. M., III, Rong, P. P., Hervig, M. E., Siskind, D. E., Stevens, M. H., Bailey, S. M., & Gumbel, J. (2014). Analysis of northern midlatitude noctilucent cloud occurrences using satellite data and modeling. *Journal of Geophysical Research: Atmospheres*, *119*(6), 3238–3250. https://doi.org/10.1002/2013JD021017

SABER. (2023). The sounding of the atmosphere using Broadband emission Radiometry instrument data (Version 2.0) [Dataset]. Retrieved from http://saber.gats-inc.com

Salby, M. L., Sassi, F., Callaghan, P., Wu, D., Keckhut, P., & Hauchecorne, A. (2002). Mesospheric inversions and their relationship to planetary wave structure. *Journal of Geophysical Research*, *107*(D4), 4041. https://doi.org/10.1029/2001JD000756

Simkhada, D. B., Snively, J. B., Taylor, M. J., & Franke, S. J. (2009). Analysis and modeling of ducted and evanescent gravity waves observed in the Hawaiian airglow. *Annales Geophysicae*, *27*(8), 3213–3224. https://doi.org/10.5194/angeo-27-3213-2009

Smith, S. M., Friedman, J., Raizada, S., Tepley, C., Baumgardner, J., & Mendillo, M. (2005). Evidence of mesospheric bore formation from a breaking gravity wave event: Simultaneous imaging and lidar measurements. *Journal of Atmospheric and Solar-Terrestrial Physics*, *67*(4), 345–356. https://doi.org/10.1016/j.jastp.2004.11.008

States, R. J., & Gardner, C. S. (2000). Thermal structure of the mesopause region (80–105 km) at 40°N latitude. Part II: Diurnal variations. *Journal of the Atmospheric Sciences*, *57*(1), 78–92. https://doi.org/10.1175/1520-0469(2000)057<0078:tsotmr>2.0.co;2

Thurairajah, B., Bailey, S. M., Nielsen, K., Randall, C. E., Lumpe, J. D., Taylor, M. J., & Russell III, J. M. (2013). Morphology of polar mesospheric clouds as seen from space. *Journal of Atmospheric and Solar-Terrestrial Physics*, *104*, 234–243. https://doi.org/10.1016/j.jastp.2012.09.009

Thurairajah, B., Bailey, S. M., Siskind, D. E., Randall, C. E., Taylor, M. J., & Russell III, J. M. (2013). Case study of an ice void structure in polar mesospheric clouds. *Journal of Atmospheric and Solar-Terrestrial Physics*, *104*, 224–233. https://doi.org/10.1016/j.jastp.2013.02.001

Thurairajah, B., Cullens, C. Y. S. M., & Bailey, S. M. (2021). Characteristics of a mesospheric front observed in polar mesospheric cloud fields. *Journal of Atmospheric and Solar-Terrestrial Physics*, *218*, 105627. https://doi.org/10.1016/j.jastp.2021.105627

Whiteway, J. A., & Carswell, A. I. (1995). Lidar observations of gravity wave activity in the upper stratosphere over Toronto. *Journal of Geophysics Research*, *100*(D7), 14113–14124. https://doi.org/10.1029/95JD00511

Yue, J., She, C.-Y., Nakamura, T., Hurrell, S., & Yuan, T. (2010). Mesospheric bore formation from large-scale gravity wave perturbations observed by collocated all-sky OH imager and sodium lidar. *Journal of Atmospheric and Solar-Terrestrial Physics*, *72*(1), 7–18. https://doi.org/10.1016/j.jastp.2009.10.002

Zhao, Y., Taylor, M. J., Randall, C. E., Lumpe, J., Siskind, D., Bailey, S., & Russell III, J. (2015). Investigating seasonal gravity wave activity in the summer polar mesosphere. *Journal of Atmospheric and Solar-Terrestrial Physics*, *127*, 8–20. https://doi.org/10.1016/j.jastp.2015.03.008